Effect of Exhaust Plume/Afterbody Interaction on Installed Scramjet Performance

T. A. Edwards*
NASA Ames Research Center, Moffett Field, California 94035

An upwind, implicit Navier-Stokes computer program has been applied to hypersonic exhaust plume/afterbody flowfields. The capability to solve typical geometries at hypersonic speeds, including an interacting exhaust plume, has been demonstrated on a simplified nozzle/afterbody model. Comparison of the numerical results with available experimental data shows good agreement in all cases investigated. For moderately underexpanded jets, afterbody forces were found to vary linearly with the nozzle exit pressure. Coupling a species continuity equation to the Navier-Stokes equations enabled calculations that indicated that exhaust gases with low isentropic exponents γ contribute up to 25% more force than high γ exhaust gases. Nozzle geometry was also found to have a large influence on the afterbody flowfield.

Nomenclature

A, B, C = flux Jacobian matrices
a = speed of sound
c = mass fraction of chemical species
c_n = normal force coefficient
c_p = specific heat at constant pressure
c_v = specific heat at constant volume
d = nozzle diameter
E, F, G = flux vectors
e = total energy
J = Jacobian of transformation
M = Mach number
Pr = Prandtl number
p = pressure
Re = Reynolds number
t, x, y, z = independent variables (time and Cartesian coordinates)
u, v, w = velocity components in x, y, z directions, respectively
α = angle of attack
γ = ratio of specific heats
$\tilde{\gamma}$ = effective γ for a gas mixture
ϵ = afterbody upsweep angle
μ = coefficient of viscosity
ρ = density
τ, ξ, η, ζ = transformed coordinates

Subscripts

e = nozzle exit conditions
i, j, k = indices in ξ, η, ζ directions, respectively
∞ = freestream conditions

Superscripts

$+, -$ = flux-split direction for flux Jacobians

Introduction

HYPERSONIC flight is a vital link in the advancement of transportation within and beyond the Earth's atmosphere. Whether it requires the relatively short exposure of a re-entry vehicle or the prolonged cruise of a hypersonic transport, surviving the aerothermodynamic environment characteristic of this flight regime constrains the design of a wide class of aerospace vehicles. This paper studies the details of one important determinant of a hypersonic vehicle's performance: impingement of the engine exhaust plume on the underbody. Since the exhaust is, in general, highly underexpanded, it exerts high pressure on the lower surface of the afterbody, which translates into additional thrust. However, small deviations from design conditions could lead easily to inadequate engine performance. Predicting performance at and away from the design point is critical to a successful design.

Integrating airframe and propulsion systems in transonic and supersonic flight has been an area of active research over the past decade. For a review of current literature on this subject, the reader is recommended to Ref. 1. Significant progress has also been made recently in the area of rocket and missile base flows at supersonic speeds.[2-5] However, in comparison to the deliberate progress seen in transonics and supersonics, research in hypersonics has been slow until recently. Activity declined sharply in the early 1970s following the successful completion of the Apollo program and preliminary design of the Space Shuttle. Hypersonics research underwent a decade-long hiatus, which was brought to an end within the last few years by the technological requirements of a new generation of hypersonic flight vehicles, such as the National Aero-Space Plane (NASP).

In an effort to make up for lost time, experimental facilities are being revitalized, from shock tubes and ballistic ranges to hypersonic wind tunnels and arcjets. Because of the importance of this research to national security, only a few current experimental results in the hypersonic regime are available in open literature. Lockman et al.[6] are presently studying the unclassified hypersonic all-body vehicle in the NASA Ames 3.5-ft hypersonic tunnel. Lockheed has tested a generic hypersonic vehicle at transonic and supersonic Mach numbers in a power-on simulation. Regardless of the availability of such data, ground-based test facilities pose an overriding shortcoming: very few of them are capable of simulating the high altitudes, Mach numbers, and Reynolds numbers of actual flight conditions. Computational fluid dynamics (CFD) is poised to supply that capability.

The past decade has been witness to a meteoric advancement in CFD capabilities. A synergistic coupling of improvements in computer resources[7] and numerical solution algorithms[8-10] has resulted in progressively faster, more accurate, less expensive flow solutions. Numerous codes have demonstrated solutions for viscous flow about realistic three-

Received June 26, 1989; revision received May 10, 1990; accepted for publication June 14, 1990.

*Assistant Chief, Applied Computational Fluids Branch. Member AIAA.

dimensional geometries at transonic and supersonic speeds.[11,12] The biggest obstacle in using these codes to solve hypersonic flows has been capturing the strong shock waves associated with the forward-facing surfaces. Development of upwind and total-variation-diminishing (TVD) algorithms[13–17] has ameliorated this problem substantially, bringing forth a generation of robust codes capable of solving hypersonic flows.[18,19]

The goal of the present work is to demonstrate a CFD capability to solve complex nozzle/afterbody problems in hypersonics and to investigate the fluid dynamics of under-expanded exhaust plumes as they impinge on vehicle afterbodies. First, a brief description of the governing equations and numerical methods is presented. Then, flow solutions for a simplified nozzle/afterbody model are presented and compared to the experimental data. Finally, the sensitivity of nozzle performance to several parameters is assessed.

Governing Equations and Numerical Methods

Navier-Stokes Equations

The thin-layer, Reynolds-averaged Navier-Stokes equations provide a good model for the flowfields considered here. Transforming these equations from Cartesian coordinates to generalized curvilinear coordinates allows solid surfaces to be mapped to constant coordinate surfaces, thereby allowing the thin-layer approximation to be invoked for arbitrarily oriented surfaces. The thin-layer Navier-Stokes equations written in generalized curvilinear coordinates are

$$\partial_\tau \hat{Q} + \partial_\xi \hat{E} + \partial_\eta \hat{F} + \partial_\zeta \hat{G} = Re^{-1}\partial_\zeta \hat{S} \tag{1}$$

where

$$\hat{Q} = J^{-1}\begin{bmatrix} \rho \\ \rho u \\ \rho v \\ \rho w \\ e \end{bmatrix} \tag{2a}$$

$$\hat{E} = J^{-1}\begin{bmatrix} \rho U \\ \rho u U + \xi_x p \\ \rho v U + \xi_y p \\ \rho w U + \xi_z p \\ U(e+p) - \xi_t p \end{bmatrix} \tag{2b}$$

$$\hat{F} = J^{-1}\begin{bmatrix} \rho V \\ \rho u V + \eta_x p \\ \rho v V + \eta_y p \\ \rho w V + \eta_z p \\ V(e+p) - \eta_t p \end{bmatrix} \tag{2c}$$

$$\hat{G} = J^{-1}\begin{bmatrix} \rho W \\ \rho u W + \zeta_x p \\ \rho v W + \zeta_y p \\ \rho w W + \zeta_z p \\ W(e+p) - \zeta_t p \end{bmatrix} \tag{2d}$$

In these equations, ξ_x, ξ_y, etc., represent the transformation metrics. The contravariant velocity components U, V, and W are defined as

$$U = \xi_t + \xi_x u + \xi_y v + \xi_z w \tag{3a}$$

$$V = \eta_t + \eta_x u + \eta_y v + \eta_z w \tag{3b}$$

$$W = \zeta_t + \zeta_x u + \zeta_y v + \zeta_z w \tag{3c}$$

The viscous flux terms are given by

$$\hat{S} = J^{-1}\begin{bmatrix} 0 \\ \mu m_1 u_\zeta + (\mu/3) m_2 \zeta_x \\ \mu m_1 v_\zeta + (\mu/3) m_2 \zeta_y \\ \mu m_1 w_\zeta + (\mu/3) m_2 \zeta_z \\ \mu m_1 m_3 + (\mu/3) m_2 (\zeta_x u + \zeta_y v + \zeta_z w) \end{bmatrix} \tag{4}$$

where

$$m_1 = \zeta_x^2 + \zeta_y^2 + \zeta_z^2 \tag{5a}$$

$$m_2 = \zeta_x u_\zeta + \zeta_y v_\zeta + \zeta_z w_\zeta \tag{5b}$$

$$m_3 = (u^2 + v^2 + w^2)/2 + Pr^{-1}(\gamma - 1)^{-1}(a^2)\zeta \tag{5c}$$

In the foregoing equations, density is nondimensionalized by ρ_∞, Cartesian velocity components are nondimensionalized by $a_\infty/\sqrt{\gamma}$, and energy by p_∞. An algebraic turbulence model[20] is used to calculate the turbulent eddy viscosity.

Pressure is related to the conservative flow variables $\hat{Q}$ by the ideal gas equation of state

$$p = (\gamma - 1)[e - \tfrac{1}{2}\rho(u^2 + v^2 + w^2)] \tag{6}$$

The metric terms are defined as

$$\xi_x = J(y_\eta z_\zeta - y_\zeta z_\eta), \qquad \eta_x = J(z_\xi y_\zeta - y_\xi z_\zeta) \tag{7a}$$

$$\xi_y = J(z_\eta x_\zeta - z_\zeta x_\eta), \qquad \eta_y = J(x_\xi z_\zeta - z_\xi x_\zeta) \tag{7b}$$

$$\xi_z = J(x_\eta y_\zeta - y_\eta x_\zeta), \qquad \eta_z = J(y_\xi x_\zeta - x_\xi y_\zeta) \tag{7c}$$

$$\zeta_x = J(y_\xi z_\eta - z_\xi y_\eta), \qquad \xi_t = -x_\tau \xi_x - y_\tau \xi_y - z_\tau \xi_z \tag{7d}$$

$$\zeta_y = J(z_\xi x_\eta - x_\xi z_\eta), \qquad \eta_t = -x_\tau \eta_x - y_\tau \eta_y - z_\tau \eta_z \tag{7e}$$

$$\zeta_z = J(x_\xi y_\eta - y_\xi x_\eta), \qquad \zeta_t = -x_\tau \zeta_x - y_\tau \zeta_y - z_\tau \zeta_z \tag{7f}$$

and

$$J = [x_\xi y_\eta z_\zeta + x_\zeta y_\xi z_\eta + x_\eta y_\zeta z_\xi - x_\xi y_\zeta z_\eta - x_\eta y_\xi z_\zeta - x_\zeta y_\eta z_\xi]^{-1} \tag{8}$$

defines the independent variable transformation Jacobian.

Species Continuity Equation

The gas leaving the scramjet nozzles is highly energized and consists of a mixture of fuel, combustion products, and the air that passes through the engine. It possesses markedly different thermodynamic properties than the external flow, and these must be accounted for in the governing equations to simulate a scramjet plume flowfield properly. As a first approximation, it is assumed that the chemical composition of the exhaust flow remains fixed after leaving the nozzle. This approximation models "frozen" flow, for which the convection time is very short compared to the chemical relaxation time. It is further assumed that the exhaust gases can be lumped together as a single species and the external flow as a second species. Thus, the flow consists of two streams of gases that have constant, but different, isentropic exponents. To account for the difference in thermodynamic properties of the two gases, a species continuity equation is solved in conjunction with the Navier-Stokes equations. The diffusion terms are neglected because their effect on overall afterbody forces is negligible compared to the convective terms. Moreover, since the equation is solved loosely coupled to the Navier-Stokes equations, it is convenient to cast it in a nonconservative form. Thus, the species continuity equation is written as

$$\frac{\partial c}{\partial t} + u\frac{\partial c}{\partial x} + v\frac{\partial c}{\partial y} + w\frac{\partial c}{\partial z} = 0 \tag{9}$$

For binary mixtures, only one species equation needs to be solved. That information, in conjunction with the global continuity equation, provides closure. Transforming Eq. (9) to generalized curvilinear coordinates gives

$$\frac{\partial c}{\partial t}+U\frac{\partial c}{\partial \xi}+V\frac{\partial c}{\partial \eta}+W\frac{\partial c}{\partial \zeta}=0 \tag{10}$$

The species continuity equation is coupled to the Navier-Stokes equations through γ. After determining the species concentrations by solving the species continuity equation, the equivalent γ, designated $\tilde{\gamma}$, is found from

$$\tilde{\gamma}=\frac{cc_{p_1}+(1-c)c_{p_2}}{cc_{v_1}+(1-c)c_{v_2}} \tag{11}$$

where the subscript 1 refers to the exhaust gas properties and 2 to the external flow properties. The ideal gas equation of state remains unchanged except that γ is replaced by $\tilde{\gamma}$:

$$p=(\tilde{\gamma}-1)[e-\tfrac{1}{2}\rho(u^2+v^2+w^2)] \tag{12}$$

Numerical Methods

The present work is an outgrowth of the UWIN (Up Wind) code, which was developed by Rai and Chakravarthy[17] as a time-dependent Navier-Stokes code compatible with parabolized Navier-Stokes (PNS) codes. The algorithm employs Steger-Warming flux splitting[13] for the implicit flux terms and the Osher upwind TVD scheme[17] for the implicit fluxes. The implicit terms are factored approximately, and if the viscous terms are temporarily omitted from Eq. (1), the system can be written

$$\begin{aligned}&\left[I+\frac{\Delta\tau}{\Delta\xi}(\Delta_\xi A^- +\nabla_\xi A^+)\right]\left[I+\frac{\Delta\tau}{\Delta\eta}(\Delta_\eta B^- +\nabla_\eta B^+)\right]\\&\times\left[I+\frac{\Delta\tau}{\Delta\zeta}(\Delta_\zeta C^- +\nabla_\zeta C^+)\right]\Delta\hat{Q}\\&=-\Delta\tau\left[\frac{\hat{E}^n_{i+1/2}-\hat{E}^n_{i-1/2}}{\Delta\xi}+\frac{\hat{F}^n_{j+1/2}-\hat{F}^n_{j-1/2}}{\Delta\eta}\right.\\&\left.+\frac{\hat{G}^n_{k+1/2}-\hat{G}^n_{k-1/2}}{\Delta\zeta}\right]\end{aligned} \tag{13}$$

where Δ represents a one-sided forward difference operator and ∇ is a one-sided backward difference operator. See Ref. 17 for more details on the UWIN algorithm. Upwind schemes such as this offer advantages over conventional central-difference schemes for hypersonic flow problems. To capture strong shocks in hypersonic flow, central-difference schemes require large amounts of user-specified artificial smoothing, which tends to degrade the accuracy of the solution. On the other hand, smoothing appears inherently in upwind schemes, enabling them to capture very strong shocks without arbitrary parameters. TVD schemes have demonstrated the ability to capture shock waves and slip surfaces in one or two grid points without oscillations.[21]

The form of the species continuity equation solved in this study results in a scalar partial differential equation. To solve this numerically, one-sided spatial differencing is applied according to the local flow velocity, and the equation is approximately factored so that it may be solved with scalar tridiagonal inversions in each of the three coordinate directions. Applying this method to Eq. (10) results in the finite difference equations

$$[I+\Delta tU\delta^u_\xi][I+\Delta tV\delta^u_\eta][I+\Delta tW\delta^u_\zeta]c^{n+1}=c^n \tag{14}$$

where δ^u is an upwind difference defined as, for example,

$$\delta^u_\xi c_i=\begin{cases}c_i-c_{i-1} & \text{if } U>0\\ \frac{1}{2}(c_{i+1}-c_{i-1}) & \text{if } U=0\\ c_{i+1}-c_i & \text{if } U<0\end{cases} \tag{15}$$

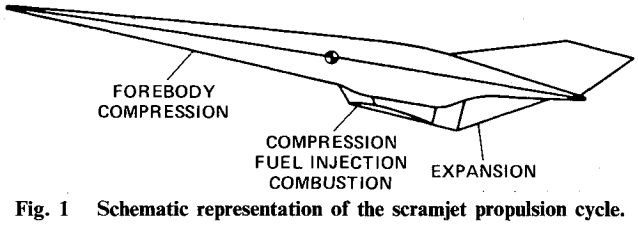

Fig. 1 Schematic representation of the scramjet propulsion cycle.

Description of Exhaust Plume Flowfields

The aerodynamics of scramjet propulsion can be described as three distinct components: 1) forebody compression, 2) internal fuel injection and ignition, and 3) afterbody expansion (see Fig. 1). Compressing the flow on the forebody is accomplished when the oncoming air traverses the bow shock of the vehicle. This creates a dense, high-pressure flow at the engine inlet, eliminating the need for the internal compressors used in turbofan and turbojet engines. The internal segment of the scramjet propulsion cycle consists of further flow compression, followed by fuel injection and ignition.

The final stage of the scramjet cycle, which is crucial to its performance, is the flow of underexpanded exhaust gases leaving the nozzle. Gross thrust for the scramjet derives from two sources: 1) the pressure and momentum flux at the nozzle exit plane itself, and 2) forces arising from fluid stress acting on the surface of the afterbody. Fluid pressure, acting normal to the afterbody surface, produces both lift and thrust, depending on the orientation of the surface. A nose-down pitching moment also results from afterbody lift. Since propulsion system lift, thrust, and moment account for a significant fraction of the overall forces on the hypersonic vehicle, effectively utilizing the afterbody will play an important role in maximizing propulsion system performance. The afterbody design—both its geometry and material composition—will determine whether the energy in the fluid (kinetic, thermal, and chemical) is extracted to generate additional propulsive forces or is left behind in the wake.

To study the effects of exhaust plume/afterbody interactions and calibrate the numerical method, a generic nozzle/afterbody model was analyzed. This model provided data on the sensitivity of afterbody forces to some governing parameters, such as nozzle exit pressure ratio and exhaust gas properties, and served to validate the numerical solutions. These results are presented and discussed.

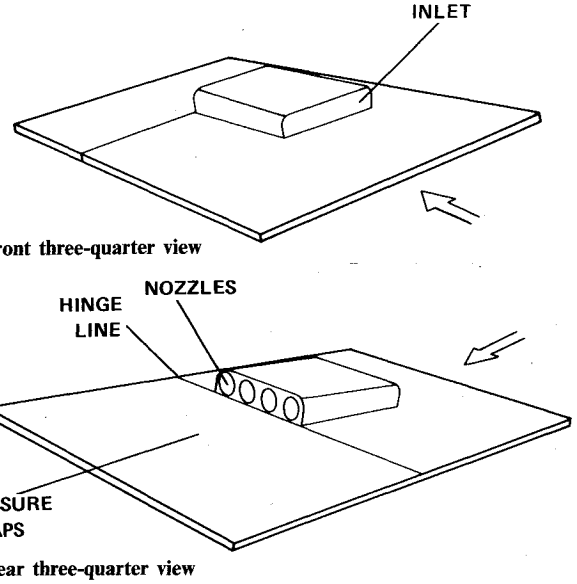

a) Front three-quarter view

b) Rear three-quarter view

Fig. 2 Nozzle/afterbody model geometry.

Nozzle/Afterbody Model

The experimental model considered here was analyzed by Cubbage and Kirkham[22] in the late 1960s and had as its goal the measurement of the lift, drag, and pitching moment increments resulting from the impingement of an underexpanded exhaust plume on a flat plate. The model, pictured in Fig. 2, consists of an inlet/nozzle assembly attached to a flat plate that represents a simplified hypersonic vehicle underbody. The plate is hinged at the nozzle exit plane to simulate varying afterbody upsweep angles. The afterbody portion of the model measures 17.78 cm long by 25.4 cm wide. The nozzle assembly is 9.14 cm wide and 2.29 cm high. Boundary-layer trips were placed approximately 3 cm downstream of the leading edge to insure turbulent flow over the rest of the body. The tests were conducted in the Langley 20-in. Mach 6 tunnel at a stagnation pressure of 25 atm and a stagnation temperature of 480 K. The Reynolds number was 20.9×10^6/m. Instrumentation consisted of pressure taps placed in a grid pattern downstream of the nozzle assembly in the jet expansion region.

Two axisymmetric nozzle geometries were tested with the flat plate model, one of which was designed for air ($\gamma = 1.4$) and the other for a gas mixture of 75% sulfur hexafluoride (SF_6) and 25% nitrogen (N_2) by weight, which yields $\gamma = 1.26$ at the nozzle exit plane. This mixture was chosen because it is relatively inert and stable, producing a dense, energetic gas akin to frozen flow in an actual flight condition. The nozzles were designed to produce nearly the same momentum flux and Mach number at the nozzle exit plane for both gases, and both had an exit diameter of 2.03 cm. A two-dimensional, or slot nozzle was also tested with air as the exhaust gas. The width of the slot nozzle was the same as the width of the axisymmetric nozzle assembly, 9.14 cm. The height of the slot nozzle was 1.52 cm. Air flowing into the inlet of the nozzle assembly was exhausted outside the test section, while the nozzle flow was supplied by a high pressure reservoir. Pressure data were reported along the model centerline (between the two inner nozzles) and on the centerline of an outboard nozzle. Normal forces on the plate were computed by discrete integration of the pressure data.

The nozzle/afterbody geometry lent itself naturally to a Cartesian grid topology, which was generated algebraically. Geometric stretching clustered grid points near the solid surfaces. The first grid point above the plate surface was placed 0.001 cm away, which resulted in an average y^+ of about 2.5. Figure 3 shows a perspective view of the grid topology. This overall grid was divided into two streamwise segments to reduce the computer memory requirement. Zone 1 had 32 points in the stream direction, 33 points across the semispan, and 62 points in the plate-normal direction, whereas zone 2 had 31, 33, and 62, respectively. Excluding the overlapping planes between zones, the grid totalled 122,760 points. The zonal interfaces are one to one, and no interpolation was necessary to pass information between the zones.

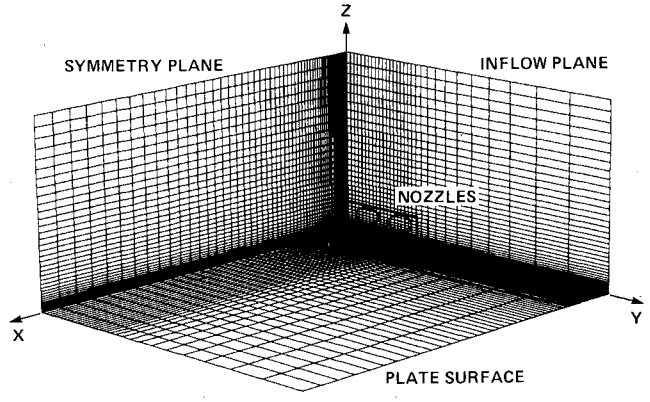

Fig. 3 Cartesian grid topology for nozzle/afterbody model.

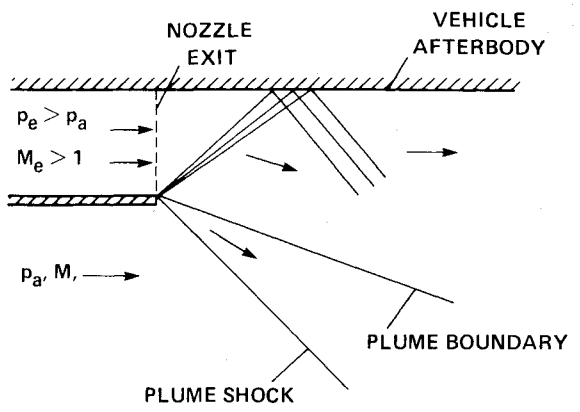

Fig. 4 Schematic of an underexpanded jet flowfield.

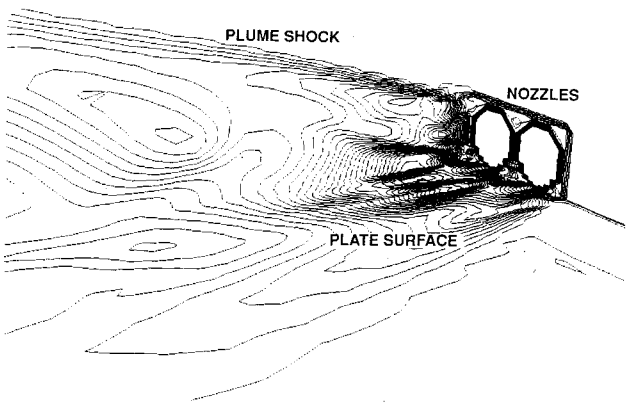

Fig. 5 Perspective view of pressure contours on plate surface, at the symmetry plane, and at the inflow plane of the nozzle/afterbody model: $M_\infty = 6$, $\alpha = 5$ deg, $p_e/p_\infty = 6.23$.

The solution domain includes only that part of the plate downstream of the exhaust nozzles. The nozzle geometry was not modeled explicitly in the grid; rather, the effect of the nozzle flow (and surrounding solid surfaces) was accounted for through the inflow boundary conditions. Specifically, a logical array was defined for the inflow plane that determined the type of boundary condition to apply at each point in that plane. The boundary condition represented either 1) nozzle exhaust conditions, 2) turbulent flat plate conditions (from a previously calculated flowfield), or 3) solid surface conditions, depending on the location of the particular grid point in the inflow plane. Fully turbulent flow was assumed at the inflow plane.

To facilitate later discussions, it is helpful first to describe the important features of an underexpanded jet flow. A jet is termed underexpanded when the static pressure at the nozzle exit plane is greater than the ambient static pressure. Upon leaving the nozzle, the flow expands by turning toward the region of lower pressure, as shown in Fig. 4. The adjacent supersonic external flow is forced to turn also, and an oblique shock wave (the plume shock) emanates from the nozzle lip. Meanwhile, an expansion fan propagates into the plume flow, eventually contacting and reflecting off of the afterbody surface. For two-dimensional and axisymmetric flows, waves continue to reflect off of the contact surface and nozzle centerline, giving rise to the diamond pattern sometimes seen in rocket plumes. For nonaxisymmetric geometries, waves propagate out of phase with one another. The ensuing nonsimple wave interactions dissipate the pressure gradients through fluid viscosity, and so the wave structure is less apparent.

This flow pattern is evident in the numerical solutions. For example, Fig. 5 shows the calculated pressure contours on the plate, at the symmetry plane of the model, and at the inflow

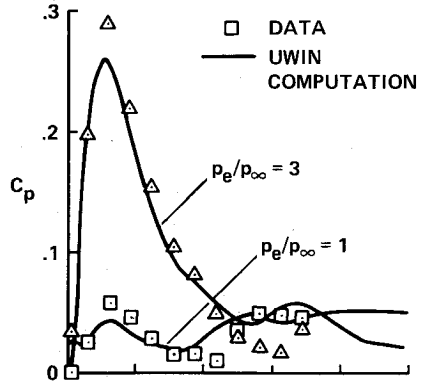

a) Between nozzles

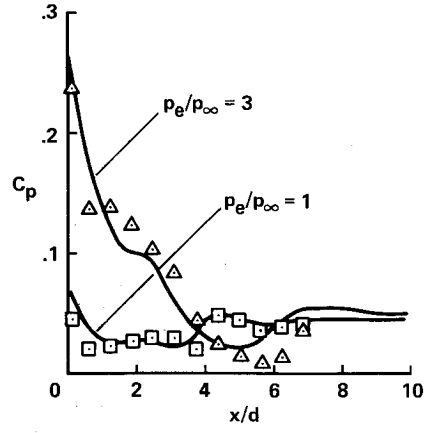

b) Nozzle centerline

Fig. 6 Comparison of calculated and experimental surface pressure coefficients for nozzle/afterbody model: $M_\infty = 6$, $\alpha = 5$ deg.

plane. Flow conditions for this solution were $M_\infty = 6$, $\alpha = 0$ deg, $Re = 2.09 \times 10^5\ \text{cm}^{-1}$, and $\epsilon = 0$ deg. The nozzle exit pressure ratio is 6.23, and the exit Mach number is 3.5. At the inflow plane, pressure contours outline the nozzle circumferences. As described earlier, a Cartesian grid topology was employed with explicit inflow boundary conditions. The discrete representation of the round nozzles is evident from the pattern of pressure contours at the inflow plane. The plume shock is also readily evident in this view at the symmetry plane. Pressure peaks on the plate are apparent near the nozzle lip (where the exhaust flow first impinges on the plate) and further downstream where adjacent plumes interact.

Surface pressure coefficients are compared with the experimental data at two pressure ratios in Figs. 6. In Fig. 6a, the pressure along the model centerline is seen first to rise due to a shock impingement at $x/d \approx 1.5$, then fall to near ambient pressure at $x/d \approx 5$. The shock is the result of adjacent plumes interfering with one another as they expand to ambient pressure. Further downstream, the flow overexpands, and at $x/d \approx 6$, a recompression is apparent. The comparison in this figure is generally good, though the strength of the first shock is underpredicted somewhat. This is due in part to the discrete modeling of the round nozzles, as will be shown later in a study of grid refinement: more accurate modeling of the nozzle results in greater interference and a higher pressure peak. Figure 6b shows the surface pressure coefficients on the centerline of the outboard nozzle. The pressure falls rapidly from its value at the exit plane, then reaches a plateau that occurs at $x/d \approx 1$ in the experimental data and at $x/d \approx 2$ in the calculated result. The pressure plateau occurs where the expansion of the exhaust plume is restricted by interference with the adjacent plume. Downstream of this point, the flow becomes slightly overexpanded then recovers to ambient pressure. Discrepancies there are also attributed to grid resolution at the nozzle exit plane.

Parametric Effects on Afterbody Forces

Numerous parameters affect the magnitude and direction of force arising from the impingement of the exhaust plume on the afterbody. The simplified nozzle/afterbody model permitted analysis of some of the dominant variables. In this section, an investigation of parametric sensitivities is opened. Parameters studied include the nozzle exit pressure ratio, exhaust gas properties, and nozzle geometry. Finally, the sensitivity of the numerical results is assessed with a grid refinement study.

Pressure Ratio

Solutions for the nozzle/afterbody model were obtained at otherwise fixed operating conditions with variations in exit pressure ratio. To assess the sensitivity of the afterbody normal force to the exit pressure ratio, solutions were obtained for $p_e/p_\infty = 1$, 2, 3 and 4 at $\alpha = 0$ deg and $\epsilon = 0$ deg. Figure 7 presents incremental normal force coefficients as a function of the nozzle exit pressure ratio. To compute the incremental value, the power-off normal force coefficient is subtracted from the power-on value. The comparison of the numerical results with the data is very good, and the model exhibits a linear relationship between exit pressure and normal force, as expected. Other things equal, an increase in the nozzle exit pressure gives rise to a corresponding increase in pressure on

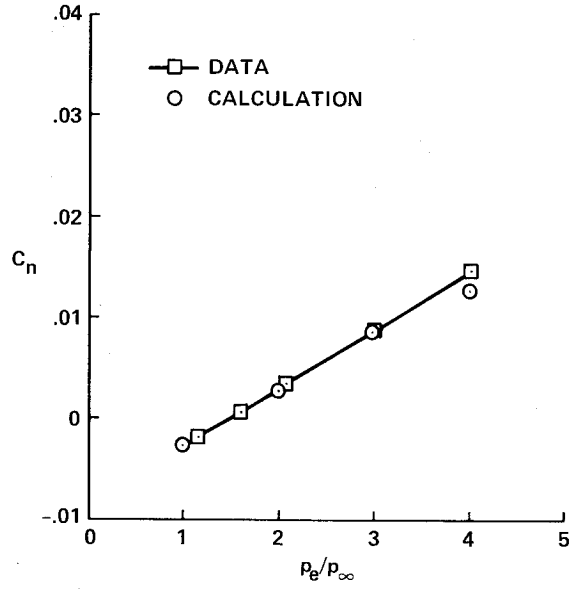

Fig. 7 Variation of normal force coefficient with exit pressure ratio: $M_\infty = 6$, $\alpha = 0$ deg.

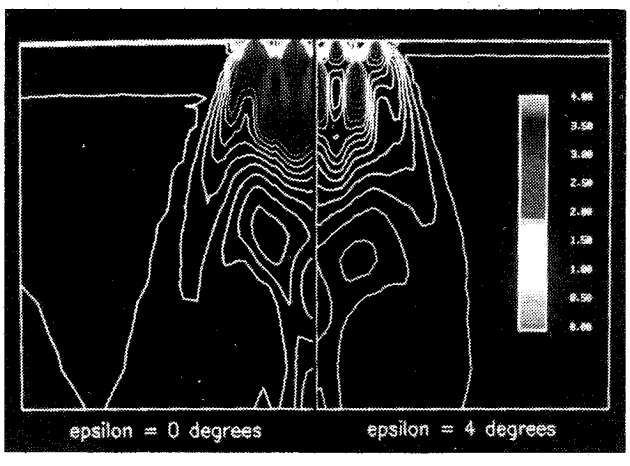

Fig. 8 Comparison of surface pressure contours for different exhaust gases: $M_\infty = 6$, $\alpha = 0$ deg, $p_e/p_\infty = 4$.

Table 1 Effect of grid density on plate normal force

Grid	Dimensions i	j	k	Total points	c_n
Coarse	31	17	31	16,337	0.1009
Medium	60	33	62	122,760	0.1256
Fine	119	63	123	922,131	0.1362

$M_\infty = 6$, $\alpha = 5$ deg, $\epsilon = 0$ deg, $p_e/p_\infty = 6.23$.

the region of the plate downstream of the nozzles. Hence, the force on the plate rises in direct proportion to the nozzle exit pressure.

Exhaust Gas Properties

The partially burned exhaust gases leaving a scramjet nozzle will exhibit different thermodynamic properties than the surrounding air. Coupling a species continuity equation to the Navier-Stokes equations made it possible to assess the effects that different (ideal) exhaust gases have on the afterbody forces. In this experiment, an exhaust gas mixture of 75% sulfur hexafluoride (SF_6) and 25% nitrogen (N_2), for which $\gamma_e = 1.26$, was compared to the results for air. Since SF_6 has more internal energy modes than air, it requires a greater volumetric expansion to achieve a given pressure drop.

Figure 8 shows the effect this has on the afterbody flowfield. At $\alpha = 0$ deg, $\epsilon = 0$ deg, and $p_e/p_\infty = 4$, the footprint for SF_6 exhaust gas is notably larger than for air: it persists an additional nozzle diameter downstream and spreads laterally by about another one-half nozzle diameter. The pressure within the SF_6 footprint is higher as well; for this case, the incremental normal force for $\gamma_e = 1.26$ was about 25% higher than for $\gamma_e = 1.4$. Comparisons of the calculated and measured normal force coefficient at several exit pressure ratios are shown in Fig. 9. The variation of normal force coefficient with exit pressure ratio is still linear, but the slope is about 30% greater for $\gamma_e = 1.26$ than for $\gamma_e = 1.4$. Therefore, at the same exit conditions, a gas with a low value of γ will produce greater afterbody forces than one with a high value of γ.

Nozzle Geometry

In Fig. 5, it can be seen that adjacent axisymmetric nozzles leave regions of stagnant flow near the exit plane. This

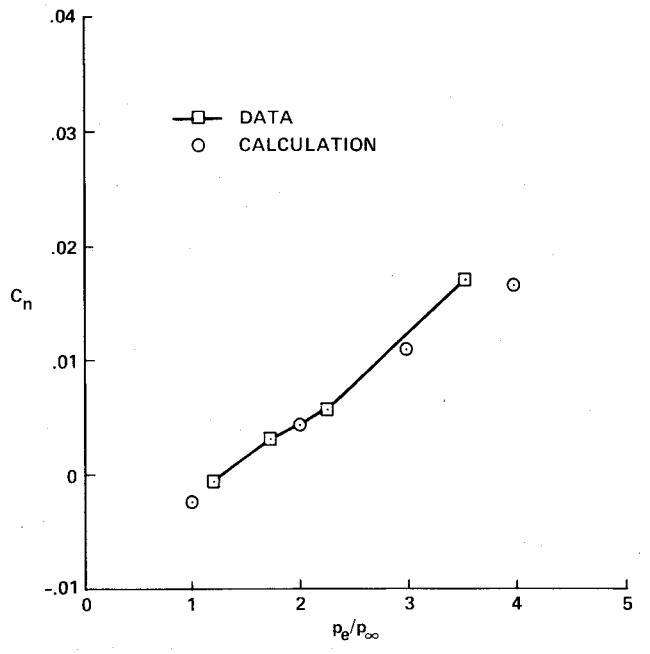

Fig. 9 Variation of normal force coefficient with exit pressure ratio for SF_6 exhaust gas: $M_\infty = 6$, $\alpha = 0$ deg.

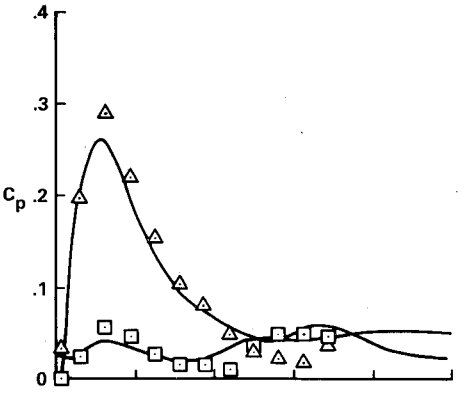

a) Axisymmetric nozzles

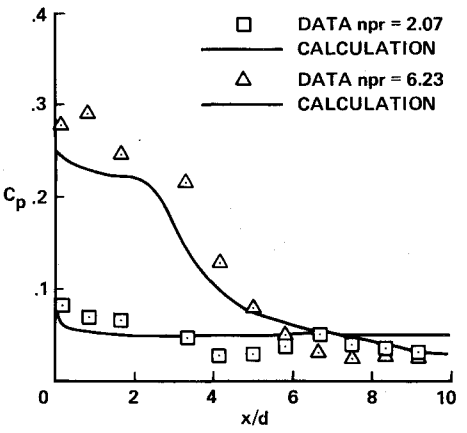

b) Slot nozzle

Fig. 10 Comparison of calculated and experimental surface pressure coefficients for axisymmetric and slot nozzle geometries: $M_\infty = 6$, $\alpha = 5$ deg.

observation leads to the question: Does a nozzle geometry that produces a cleaner flowfield near the exit generate greater afterbody forces? To investigate this, an alternate slot nozzle was tested. The dimensions of the slot nozzle model were determined by specifying the overall width of the nozzle assembly to remain the same. The nozzle height was then fixed so as to produce the same momentum flux through the slot nozzle as the four axisymmetric nozzles at the same exit conditions. Test conditions for the comparison were $\alpha = 5$ deg, $\epsilon = 0$ deg, and $p_e/p_\infty = 6.23$.

Comparisons of the calculated surface pressure coefficients with experimental data[22] are shown in Figs. 10. Centerline pressure for the slot nozzle is seen to be consistently underpredicted from $x/d = 0$ to $x/d \approx 5$. This is thought to be a result of two discrepancies between the experiment and the numerical model: 1) nonuniform experimental exit flow conditions, causing a pressure peak near the exit face, and 2) geometrical disparity, causing the predicted onset of expansion to occur about one nozzle diameter upstream of the experimentally determined location.

The flow pattern near the plate renders a clearer visualization of why the two nozzle geometries perform differently. Figure 11 presents limiting streamlines for the two nozzle geometries. The slot nozzle produces a virtually two-dimensional flowfield away from the edges of the nozzle assembly. The flow is, indeed, much cleaner than the axisymmetric geometry, showing no recirculating flow near the nozzle exit. This has a significant effect on the afterbody normal force: for the slot nozzle, $c_n = 0.0778$, whereas for the axisymmetric nozzle, $c_n = 0.0409$.

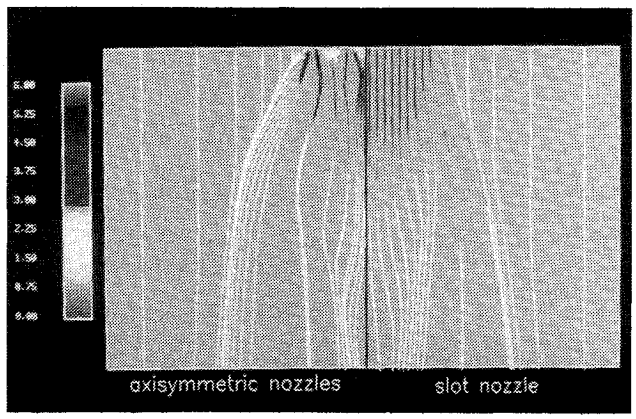

Fig. 11 Comparison of limiting streamlines colored by pressure near nozzle exit for axisymmetric and slot nozzle geometries: $M_\infty = 6$, $\alpha = 5$ deg, $p_e/p_\infty = 6.23$.

Grid Resolution Effects

As a necessary final step to the nozzle/afterbody investigation, the convergence of the numerical results is tested on refined grids. Obtaining numerical solutions on a series of grids measures the accuracy and uniqueness of the results. The value of relevant flowfield variables should approach a limit asymptotically as the grid is refined. To minimize the effects of grid stretching on the results of this study, results were first obtained on a fine grid, which was then coarsened twice by discarding alternate grid points in each of the three coordinate directions. Though this technique does not preserve *identical* stretching on the coarsened grid, it does produce geometrically similar grid cells from one grid to the next. Discarding alternate grid cells in all three directions results in an eightfold reduction in the total number of grid points. The fine grid dimensions were 119 points in the streamwise direction, 63 in the spanwise direction, and 123 in the plate-normal direction, for an overall total of 922,131 points. Hence the medium grid dimensions were 60, 33, and 62 points, respectively, for a total of 122,760 points; the coarse grid had 31, 17, and 31 points, respectively, for a total of 16,337 points.

Pressure coefficient comparisons among solutions on the three grids are shown in Figs. 12. The coarse grid result follows the broad trends in the data, but fails to place the interference peak correctly in Fig. 12a, and shows no evidence of recompression at $x/d = 6$. The medium and fine grid results are nearly identical to one another, the only noteworthy difference being that the fine grid result shows a higher interference peak (Fig. 12a). Figure 12b shows similar trends.

Figures 13 compare boundary-layer profiles at $x/d = 1$ among the solutions. The profiles between adjacent nozzles, Fig. 3a, show some differences in the solutions. The coarse grid predicts attached flow at this station, whereas the medium and fine grids show significant reverse flow. The flow reversal is precipitated by the shock waves from the interaction of adjacent plumes, and the discrepancies seen in this figure are most likely a result of how well the plume interaction process is resolved. On the nozzle centerline, Fig. 13b, all of the results are identical, indicating that even the coarse grid adequately models the attached flow. To resolve the viscosity-dominated flowfield near the nozzle exit would require a grid much finer than those studied here.

However, plate force measurements would not be sensitive to further refinement of the grid. Plate normal force coefficients, shown in Table 1, indicate the asymptotic trend toward a value of about 0.138. The medium grid dimensions, which were used for the other nozzle/afterbody grids as well, appear to resolve most of the flow characteristics adequately and can be used to calculate integrated quantities to within about 10% of the asymptotic value.

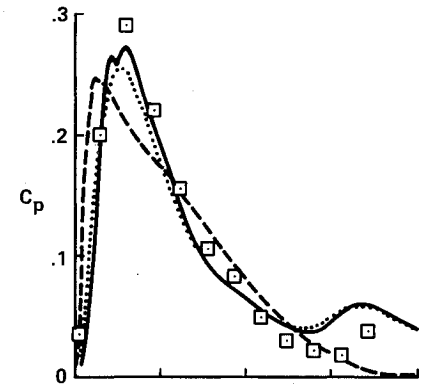

a) Between nozzles

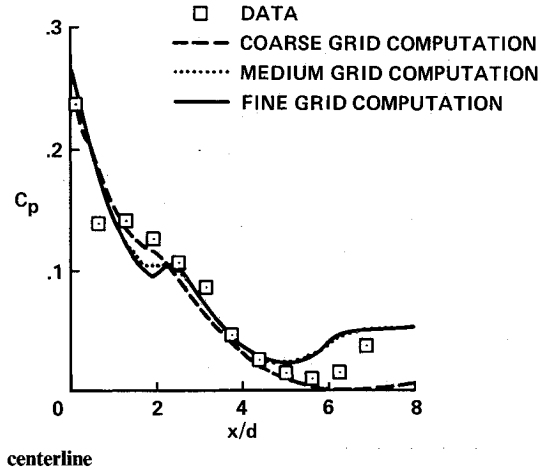

b) Nozzle centerline

Fig. 12 Comparison of calculated surface pressure coefficients on coarse, medium, and fine grids: $M_\infty = 6$, $\alpha = 5$ deg, $p_e/p_\infty = 6.23$.

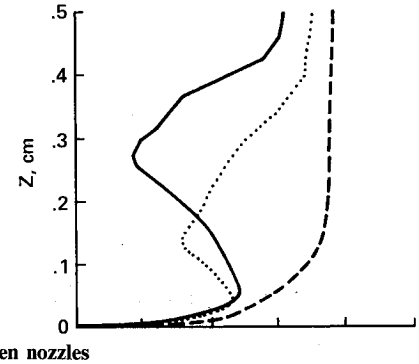

a) Between nozzles

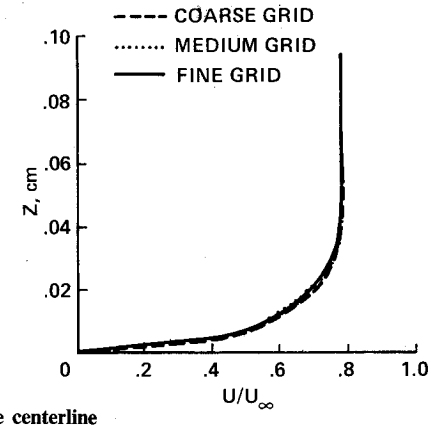

b) Nozzle centerline

Fig. 13 Comparison of calculated boundary-layer profiles at $x/d = 1$ for coarse, medium, and fine grids: $M_\infty = 6$, $\alpha = 5$ deg, $p_e/p_\infty = 6.23$.

Conclusions

The capability to solve numerically the interaction of an underexpanded exhaust plume with a vehicle afterbody has been demonstrated. The numerical results compared favorably with experimental data for several operating conditions. This confirms the viability of using component studies such as this to study parametric sensitivities of hypersonic vehicle aerodynamics. Based on the results of this investigation, the effects of exhaust plume impingement on afterbody forces can be summarized as follows:

1) At low exit pressure ratios (<10), the afterbody force varies linearly with exit pressure ratio.

2) Exhaust gases with low isentropic exponents can contribute 25% more afterbody force than high-γ gases under the same exit conditions, assuming frozen flow.

3) The nozzle geometry and initial plume development process are very important in recovering the plume energy as propulsive afterbody force.

References

[1]Mace, J., and Hankey, W., "Review of Inlet-Airframe Integration Using Navier-Stokes Computational Fluid Dynamics," AIAA Paper 84-0119, Jan. 1984.

[2]Wolf, D., Dash, S., and Pergament, H., "A Shock-Capturing Model for Two-Phase, Chemically-Reacting Flow in Rocket Nozzles," AIAA Paper 85-0306, Jan. 1985.

[3]Venkatapathy, E., Lombard, C. K., Bardina, J., and Luh, R. C.-C., "Accurate Numerical Simulation of Supersonic Jet Exhaust Flow with CSCM on Adaptive Overlapping Grids," AIAA Paper 87-0465, Jan. 1987.

[4]Petrie, H., and Walker, B., "Comparison of Experiment and Computation for a Missile Base Region Flowfield with a Centered Propulsive Jet," AIAA Paper 85-1618, July 1985.

[5]Hoffman, J. J., Birch, S. F., Hopcroft, R. G., and Holcomb, J. E., "Navier-Stokes Calculations of Rocket Base Flows," AIAA Paper 87-0466, Jan. 1987.

[6]Lockman, W. K., Cleary, J. W., and Lawrence, S. L., "Flow Visualization and Pressure Distribution for an All-Body Hypersonic Aircraft," Fourth National Aero-Space Plane Technology Symposium, Paper 53, Feb. 1988.

[7]Chapman, D., "Computational Aerodynamics Development and Outlook," *AIAA Journal*, Vol. 17, No. 12, 1979, pp. 1293–1313.

[8]MacCormack, R., "The Effect of Viscosity in Hypervelocity Impact Cratering," AIAA Paper 69-354, 1969.

[9]Beam, R., and Warming, R., "An Implicit Finite-Difference Algorithm for Hyperbolic Systems in Conservation-Law Form," *Journal of Computational Physics*, Vol. 22, Sept. 1976, pp. 87–110.

[10]Pulliam, T., and Chaussee, D., "A Diagonal Form of an Implicit Approximate-Factorization Algorithm," *Journal of Computational Physics*, Vol. 39, No. 2, 1981, pp. 347–363.

[11]Flores, J., Chaderjian, N., and Sorenson, R., "Simulation of Transonic Viscous Flow over a Fighter-Like Configuration Including Inlet," AIAA Paper 87-1199, July 1987.

[12]Rizk, Y., and Ben-Shmuel, S., "Computation of the Viscous Flow Around the Shuttle Orbiter at Low Supersonic Speeds," AIAA Paper 85-0168, Jan. 1985.

[13]Steger, J. L., and Warming, R. F., "Flux-Vector Splitting of the Inviscid Gas Dynamic Equations with Applications to Finite Difference Methods," *Journal of Computational Physics*, Vol. 40, 1981, pp. 263–293.

[14]Roe, P., "Approximation Riemann Solvers, Parameter Vectors, and Difference Schemes," *Journal of Computational Physics*, Vol. 43, 1983, pp. 357–372.

[15]Yee, H., "On Symmetric and Upwind TVD Schemes," NASA TM-86842, Sept. 1985.

[16]Roe, P., "Generalized Formulation of TVD Lax-Wendroff Schemes," Inst. for Computer Applications in Science and Engineering, Rept. 84–53, Oct. 1984.

[17]Rai, M., and Chakravarthy, S., "An Implicit Form for the Osher Upwind Scheme," *AIAA Journal*, Vol. 24, No. 5, 1986, pp. 735–743.

[18]Lawrence, S., Tannehill, J., and Chaussee, D., "Application of an Upwind Algorithm to the Three-Dimensional Parabolized Navier-Stokes Equations," AIAA Paper 87-1112, Jan. 1987.

[19]Edwards, T., Chaussee, D., Lawrence, S., and Rizk, Y., "Comparisons of Four CFD Codes as Applied to a Hypersonic All-Body Vehicle," AIAA Paper 87-2642, Aug. 1987.

[20]Baldwin, B. S., and Lomax, H., "Thin-Layer Approximation and Algeraic Model for Separated Turbulent Flows," AIAA Paper 78-257, Jan. 1978.

[21]Yee, H. C., "Numerical Experiments with a Symmetric High-Resolution Shock-Capturing Scheme," NASA TM 88325, June 1986.

[22]Cubbage, J. M., Jr., and Kirkham, F. S., "Investigation of Engine-Exhaust-Airframe Interference on a Cruise Vehicle at Mach 6," NASA TN D-6060, Jan. 1971.